Final submitted manuscript: published in Applied Acoustics 186 (2022) 108494
doi: 10.1016/ j.apacoust.2021.108494

Comparison of vibration and noise characteristics of urban rail transit bridges with box-girder and U-shaped sections

Qi Li[1], Baorui Dai[1], Zhihui Zhu[2*], David J. Thompson[3]

[1] Department of Bridge Engineering, Tongji University
1239 Siping Road, Shanghai, China
[2] School of Civil Engineering, Central South University
932 Lushannan Road, Changsha, China
[3] Institute of Sound and Vibration Research, University of Southampton,
Southampton SO17 1BJ, United Kingdom

Abstract: Rolling noise and structure-borne noise from rail transit viaducts often lead to complaints from nearby residents. Concrete box section bridges are commonly adopted for the viaducts but those with U-shaped sections have become popular recently due to their more attractive form and reduced visual impact. One question that often arises in relation to the choice of the section types is their relative noise performance. This study aims to compare the vibration and noise characteristics of concrete bridges with different sections in a systematic way by using the same noise prediction method. A coupled track-bridge model is introduced to obtain the rail vibration and the power input to the bridge through the rail fasteners. A three-dimensional vibro-acoustic finite element method is applied to obtain the noise radiated from the bridge and the rail subjected to sets of multiple forces acting on them. This is determined in terms of the radiation efficiency and sound pressure transfer functions for arbitrary forcing. The averaged mean squared vibration velocity of the coupled wheel-track-bridge model subjected to roughness excitation is used to scale the noise from the acoustic model. The method is validated by comparison with field measurements of noise from a U-shaped bridge in Shanghai. Comparative investigations are then conducted of the U-shaped bridge, a box girder bridge with

single cell and a twin-box girder bridge with two cells; each is fitted with equivalent noise barriers. It is found in each case that the noise from the rail is about 10 dB(A) larger than the bridge noise at positions to the side of the bridge. The U-shaped girder generally leads to slightly lower total noise levels than the box girders, with differences of less than 1 dB(A) when they have noise barriers of the same height. In terms of the bridge noise, however, the single-box and twin-box girders produce an average of 8.6 and 11.7 dB(A) less noise than the U-shaped girder.

Keywords: urban rail transit; concrete bridges; vibration and noise; wheel-rail interaction; finite element method

1 Introduction

Rail transit systems are rapidly developing in China [1], with metro systems operating in at least 40 major cities and planned in more than 100 other cities. In both Shanghai and Beijing, the networks are already over 700 km in length and are continually being expanded. For such rail transit systems, viaducts are often adopted in suburban areas instead of underground tunnels for economic reasons. Concrete box section bridges are traditionally adopted for the viaducts but those with U-shaped sections have become popular recently due to their more attractive form and reduced visual impact. However, regardless of section types, high levels of rolling noise and structure-borne noise from the viaducts may lead to complaints from nearby residents. To mitigate the viaduct noise, the acoustic characteristics of bridges requires investigation.

To investigate the noise radiated from railway bridges, many methods have been proposed to combine the vibrational and acoustical parts of the noise prediction procedure. The boundary element method (BEM) is usually adopted to obtain the noise from concrete bridges; this is

applied in combination with the finite element method (FEM) which is used to compute the structural vibration. Li et al. [2] and Zhang et al. [3] both used three-dimensional (3D) train-track-bridge dynamic interaction models to obtain the bridge vibration although different approaches were adopted to calculate the sound radiation using the 3D BEM. To improve computational efficiency while keeping the 3D fidelity, Li et al. [4] proposed a two-and-a-half-dimensional (2.5D) BEM-based approach to obtain the modal acoustic transfer vectors (MATVs) for the prediction of bridge noise. Song et al. [5, 6] extended this approach to allow the prediction of noise from multi-span bridges and the investigation of both bridge and rail noise. Recently, Li and Thompson [7] used the 2.5D FEM-BEM method to evaluate the acoustic characteristics of a U-shaped concrete bridge by introducing a multilayer fastener model. Song et al. [8] combined the wavenumber FEM and 2D BEM for the rapid prediction of bridge noise.

The vibration of steel bridges is more effectively and widely obtained from statistical energy analysis (SEA), as steel structures generally have a much larger number of vibration modes than the corresponding concrete structures. The model employing SEA relies on the energy balance equations and does not require the structure to be meshed, which simplifies a complex dynamic problem to a smaller set of linear algebraic equations [9]. Remington and Wittig [10] calculated the transmission of vibration from the rails to the bridge using SEA and the sound radiation of the whole system through the radiation efficiency of each component. Janssens and Thompson [11] calculated the input acoustic power of the bridge based on the bridge point mobility and the load transmitted via the rail fasteners. They also showed that the noise from the rail can be significant for track with direct fasteners. Bewes et al. [12] presented an

improved rail and bridge model to consider the rail-bridge coupled vibration below the decoupling frequency as well as the resonance properties of the finite structure. As the SEA approach is less accurate in the low frequency range, hybrid FEM-SEA methods have been developed to predict noise radiation from structures over a wider frequency range [13, 14]. Poisson and Margiocchi [15] conducted a vibroacoustic investigation of a steel bridge using FEM below 200 Hz and SEA above 200 Hz. Liu et al. [16] used the hybrid FEM-SEA approach to investigate the noise of a steel-concrete composite bridge.

Although many prediction methods have been proposed for the noise from bridges, few studies have compared the acoustic performance of different types of bridge. Wu and Liu [17] have made comparisons between a U-shaped girder and a box girder and found that the structure-borne sound power radiated from the box girder is lower than that from the U-shaped girder but they did not discuss the rail noise. Another limitation of existing studies for bridge noise prediction is that the acoustical models used are either rather complicated, for example using waveguide BEM [7], or too simple, based on analytical expressions for the acoustic power [18, 19]. Besides, for vibration prediction most studies assumed either incoherent roughness [7, 20, 21] or coherent roughness [16, 18, 22] excitation from different wheels but these different methods have not been compared.

To address these issues, a procedure is introduced to simulate the vibration of the coupled rail-bridge system, as well as the corresponding noise radiation, with acceptable accuracy and convenience for engineering purposes. Both the incoherent and coherent roughness assumptions are included in the vibration analysis model and their results are compared. A three-dimensional acoustical model is used for the bridge and the rails. The effect of noise from

multi-span bridges is taken into account by a simple reciprocity method. This procedure is validated by comparison with field test results for a U-shaped bridge. It is then applied to a comparative study of the vibration and noise from a U-shaped bridge, a single box-girder bridge and a twin box-girder bridge. Each is fitted with direct track fastenings with the same stiffness. The structure of the paper is organized as follows. Section 2 introduces the method for calculating the vibration of the rail and bridge subjected to wheel-rail combined roughness excitation. Section 3 presents 3D acoustic models for the rail and bridge and the method to obtain the noise from multiple spans of a viaduct. Section 4 gives some examples to verify the assumptions in the vibrational and acoustical calculation, including comparison with measurements. Section 5 compares the noise performance of the three bridges with different cross-sections. Part of this work was reported in preliminary form in [23]; the current paper presents an extension and revision of that work, including a much more detailed investigation of the phenomena.

2 Vibration prediction

The vibration of a train-track-bridge system is time-varying in nature and is primarily caused by random excitation from the wheel-rail combined roughness [24]. Additionally, parametric excitation occurs from stiffness variation of the discretely supported track [25-27] as well as the bridge structures; however, this is relatively insignificant compared with the normal random roughness [24, 25] except around the pinned-pinned frequency, typically occurring at about 1 kHz. The low frequency vibration modes of the bridges, bogies and car-bodies of the train can be neglected for noise prediction. In addition, the Doppler effect in the structures can be omitted [24] because the train speed of urban rail transit systems is considerably lower than the speed

of the waves propagating in the track and bridge structures. Therefore, noise-oriented vibration analysis of the train-track-bridge systems with direct fastenings can be conducted in the frequency domain with a stationary wheel-rail-bridge model and the so-called moving roughness method [28]. The procedure used for calculating the rail and bridge vibration is summarised here, based on references [21, 24]. In these references [21, 24], the vertical wheel-rail contact forces are calculated by assuming that the wheel/rail forces are uncorrelated, whereas, both the assumptions of uncorrelated and correlated wheel-rail combined roughness are adopted in this study to calculate the vertical wheel-rail contact forces and the associated rail and bridge vibration.

2.1 Rail mobility

The wheel-rail forces are dependent on the rail mobilities which can be calculated from a model of the combined rail-bridge system coupled by rail fasteners and excited by a harmonic unit force P at the rail, as shown in Fig. 1. An infinite Timoshenko beam is used to represent each rail on the bridge, and a 3D finite element model is developed for the bridge span of interest. Although an elevated bridge usually comprises multiple simply supported girders, the influence of adjacent girders is ignored and approximately considered by a rigid foundation beneath the rail fasteners. The noise produced by multiple bridge spans will be taken into account and introduced in Section 3.3. The rail and bridge (or rigid foundation) are coupled by discrete rail fasteners which exert equal and opposite forces F_i on the rail and bridge (or foundation) at each fastener position. The rail fasteners are treated as discrete springs with constant stiffness and damping loss factor. On either side of the bridge span, the length of the

rail connected by fasteners to the foundation should be large enough for the rail vibration to become sufficiently small compared with that at the driving point.

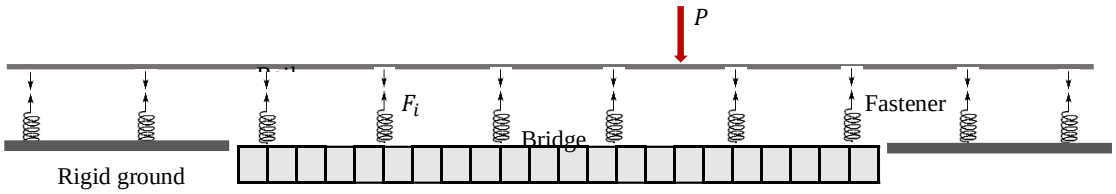

Fig. 1. Model of rail and bridge coupled by rail fasteners and excited by a harmonic force P at the rail

To find the driving point mobility and transfer mobilities of the rail, the rail-bridge model is decoupled into separate rail and bridge systems connected by the fastener forces. The mobilities of the separate rail and bridge systems are determined by the corresponding analytical or numerical models, and the unknown fastener forces are then obtained through the compatibility condition at the rail-bridge interface [21]. The mobilities of the rail when coupled to the bridge can be further obtained by summing the effects of all the fastener forces as well as the unit excitation force on the rail.

2.2 Wheel-rail interaction forces

The motion of the train is neglected in the current frequency domain analysis but different wheel/rail contact positions can be selected relative to the bridge [16, 29] to obtain the averaged responses of the wheel-rail-bridge system. Several wheels can be located on the bridge span of interest during the passage of the train. Fig. 2 shows a specific case of four wheels from two adjacent bogies on the rail-bridge system. The average vibration of the rail and bridge can be obtained using a few typical arrangements of wheels during the passage of the train. Moreover, the wheels acting on each of the two rails can be considered separately. Apart from the four

adjacent wheels, the effect of other wheels of the train can be neglected in the vibration model. This simplification will be justified in Section 4.2.

For a series of wheel/rail contacts on each rail, the vertical wheel-rail contact forces can be calculated by assuming that the wheel/rail forces are uncorrelated, using the concept of active wheels with moving vertical roughness excitation and passive wheels attached to the rail without roughness [28]. Alternatively, assuming that the wheel/rail forces are correlated, all wheels can be excited with the same roughness amplitude apart from a phase lag [16]. Both methods will be compared in this study.

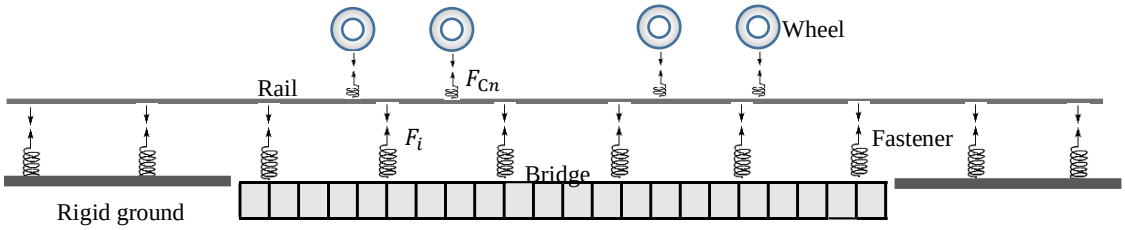

Fig. 2. Model of wheel-rail-bridge system

Regardless of the correlation of the wheel/rail forces, the wheel-rail contact forces $\mathbf{F}_c$ can be calculated based on the compatibility equation of the wheel-track-bridge system excited by moving roughness [21, 24, 30]

$$(\mathbf{Y}_r + \mathbf{Y}_c + \mathbf{Y}_w)\mathbf{F}_c = j\omega\mathbf{r} \tag{1}$$

where j is the imaginary unit; ω is the circular frequency; $\mathbf{Y}_c$ and $\mathbf{Y}_w$ are $N \times N$ matrices containing the mobilities of the wheel-rail contact spring and wheel (for a system with N wheels); $\mathbf{Y}_r$ contains the driving point and transfer mobilities of the rail under all wheels, which is obtained from Eq. (2). $\mathbf{r} = [r_1, r_2 \cdots r_N]$ is the vector of wheel-rail combined roughness amplitudes at the wheel/rail contacts.

According to concept of active wheels, the elements of $\mathbf{r}$ are zero apart from that corresponding to the *n*th wheel, and the wheel-rail contact force vector $\mathbf{F}_{\mathrm{c}}$ produced by the roughness at all the wheels can be obtained using the energy superposition principle. If, instead, the wheel-rail contact forces are calculated simultaneously by considering the roughness acting at all the wheels at the same time, the elements of $\mathbf{r}$ can be regarded as complex numbers of the same amplitude for a given wavelength of roughness, and a phase difference corresponding to the time delay between them; the rail and bridge vibration produced by all the wheels should then be summed with complex superposition rather than energy superposition. The difference between the complex and energy superposition methods for roughness excitation will be discussed in Section 4.3.

2.3 Bridge and rail vibration

Fig. 3 shows a typical case of the forces applied on the bridge through all the fasteners. As the power input to the bridge W_{b} is mainly dissipated by the structural damping of the bridge, its spatially averaged mean-square normal velocity $\langle \bar{v}^2 \rangle_{\mathrm{b}}$ can be obtained using the power balance method [24, 31]

$$\langle \bar{v}^2 \rangle_{\mathrm{b}} = \frac{W_{\mathrm{b}}}{\omega \eta M_{\mathrm{b}}} \tag{2}$$

where η is the damping loss factor and M_{b} is the mass of the bridge; ω is the circular frequency of vibration; W_{b} is produced by all the wheel-rail forces on the rail, and can be calculated using either energy superposition or complex superposition. This expression relies on there being sufficient modes in a frequency band; its application to a typical concrete bridge will be discussed in Section 4.1.

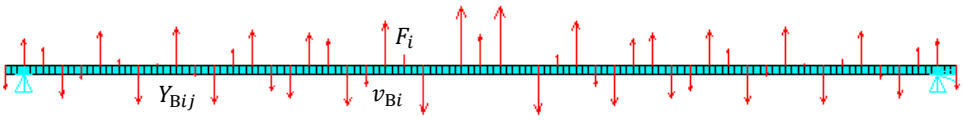

Fig. 3. Bridge model subjected to multiple fastener forces

The average vibration of the rail $\langle \bar{v}^2 \rangle_{\mathrm{r}}$ can be calculated from the fastener forces and the rail transfer mobilities over the bridge span. If the energy superposition principle is applied to account for the effects of excitation from multiple wheels, the rail vibration can be expressed as

$$\langle \bar{v}^2 \rangle_{\mathrm{r}} = \frac{k_{\mathrm{r}}}{2N_{\mathrm{f}}} \sum_{n=1}^{N} \mathbf{Y}_{\mathrm{rp},n}^{\mathrm{H}} \mathbf{Y}_{\mathrm{rp},n} F_{\mathrm{c},n}^2 \tag{3}$$

where N_{f} is the number of fasteners within the bridge span; k_{r} is a constant that represents the ratio of averaged normal velocity of the rail cross-section relative to the vertical velocity of the rail; $\mathbf{Y}_{\mathrm{rp},n}$ denotes an $N_{\mathrm{f}} \times 1$ vector of rail mobilities at each fastener position subjected to a unit force at the position of the *n*-th wheel; and $F_{\mathrm{c},n}$ is the wheel-rail contact force at the *n*-th wheel.

When the complex superposition method is applied, the rail vibration can be written as

$$\langle \bar{v}^2 \rangle_{\mathrm{r}} = \frac{k_{\mathrm{r}}}{2N_{\mathrm{f}}} \left(\sum_{n=1}^{N} F_{\mathrm{c},n} \mathbf{Y}_{\mathrm{rp},n} \right)^{\mathrm{H}} \left(\sum_{n=1}^{N} F_{\mathrm{c},n} \mathbf{Y}_{\mathrm{rp},n} \right) \tag{4}$$

3 Noise prediction

3.1 Vibro-acoustic model

Suitable acoustic models are required for the prediction of rail and bridge noise from their vibration. It is noted that the fastener forces acting on the bridge depend on the locations of the wheels on the bridge and also the track parameters. It is therefore very time-consuming if full

acoustic calculations are performed with numerical models based on the vibration of the rail and bridge obtained for fastener forces at various loading positions and for different track parameters. A more practical engineering vibro-acoustic model is therefore developed in this study to determine the radiation efficiency of the rail and bridge structures and sound transfer functions that relate the squared sound pressure at given field points to the radiated power. The radiation efficiency and sound transfer functions are assumed to be independent of the actual distribution of forces acting on the rail and bridge but are determined by their geometry and material properties. This assumption can be expected to hold because the radiation efficiency of a point-excited plate only shows significant variability below its critical frequency [32]. It is noted that the critical frequency of the concrete plates forming the bridges is very low, for example, about 70 Hz for a plate with a typical thickness of 250 mm [33]. In addition, it was also shown in reference [33] that the directivity of sound radiation from plates is mainly controlled by the wavelengths of sound waves in the air and bending waves of the plates, especially when considering the average effect of multiple forces on the plates.

Fig. 4 shows examples of three-dimensional finite element models used for vibro-acoustic calculations from one span of the rail and bridge. The acoustic analysis method proposed in this study is conducted separately for the noise of the rail and bridge, as described below. Fig. 4(a) shows the bridge structural model used for the determination of the vibrating boundary used in the acoustic model for the bridge. Harmonic analysis is performed to obtain the bridge vibration with several concentrated forces with unit amplitude but different phases applied on the bridge beneath the rail. Fig. 4(b) depicts the cross-section of a three-dimensional acoustic model of the bridge developed in the software Virtual Lab, which uses a finite element mesh for the air and

an automatic matched layer enclosing the air mesh. The size of the acoustic finite elements is determined by the software to obtain results up to 1 kHz. The acoustic calculation is conducted using the harmonic responses of the bridge surface as inputs. The effect of the ground below the bridge is omitted.

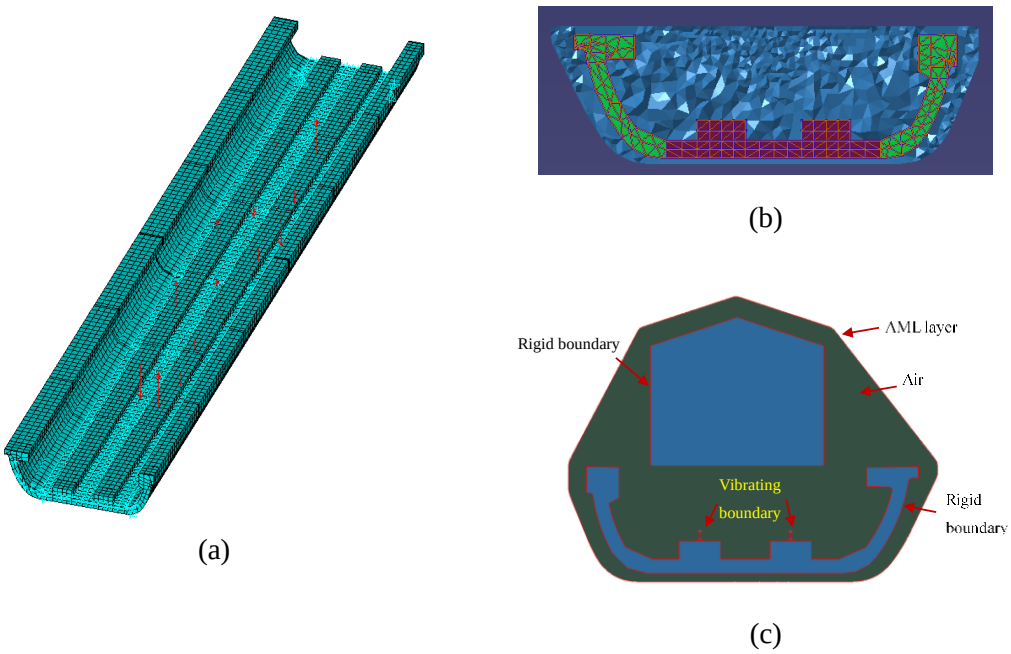

Fig. 4. An example of three-dimensional finite element models for vibro-acoustic calculation: (a) vibration model of bridge excited by assumed forces; (b) acoustic model for bridge noise; (c) acoustic model for rail noise

Fig. 4(c) shows the cross-section of a three-dimensional acoustic model of the rails developed in a similar way. It includes not only the vibrating boundary of the rails but also the reflections from both the bridge and the car-body. In reality the rails are partly supported on the rail pads and are partly above the rail bearing blocks. This complex boundary condition has some effect on the sound radiation of the rails [34]. For simplicity, in the model the rails are located above the rail bearing blocks with a gap of 60 mm, because this region forms the dominant radiation for frequencies above about 300 Hz. The vibration of the rail surface is

calculated from a discretely supported Timoshenko beams with a length of 90 m subjected to multiple unit vertical forces with arbitrary phases.

3.2 Sound power and pressure

The concept of scaling the noise from the acoustic model is employed as the basis of the noise prediction method proposed in this paper and is implemented as follows. The sound power radiated by the rail W_{sr} and by the bridge W_{sb} within one bridge span can be calculated as

$$W_{\mathrm{sr}} = \sigma_{\mathrm{r}}\rho_0 c_0 S_{\mathrm{r}}\langle\bar{v}^2\rangle_{\mathrm{r}},\ W_{\mathrm{sb}} = \sigma_{\mathrm{b}}\rho_0 c_0 S_{\mathrm{b}}\langle\bar{v}^2\rangle_{\mathrm{b}} \tag{5}$$

where S_{r} and S_{b} are the areas of the outer surface of the rail and bridge in contact with the air; ρ_0 and c_0 are the density and sound speed of the air; σ_{r} and σ_{b} are the radiation efficiencies of the rail and bridge obtained from the acoustic models excited by multiple unit forces. It is assumed the radiation efficiencies of the rail and bridge structures are not dependent on the force distribution on the structures.

Besides the radiation efficiency, the acoustic models of the rail and bridge also give the sound pressure transfer functions

$$H_{\mathrm{r},m} = \frac{\hat{p}^2_{\mathrm{r},m}}{\widehat{W}_{\mathrm{sr}}},\qquad H_{\mathrm{b},m} = \frac{\hat{p}^2_{\mathrm{b},m}}{\widehat{W}_{\mathrm{sb}}} \tag{6}$$

where the symbol $\widehat{\ }$ denotes the sound power or pressure calculated from the acoustic models of the rail and bridge subjected to a given set of unit forces; $\hat{p}^2_{\mathrm{r},m}$ and $\hat{p}^2_{\mathrm{b},m}$ are the mean square sound pressure at the field point obtained from the acoustic models of rail and bridge respectively; $H_{\mathrm{r},m}$ and $H_{\mathrm{b},m}$ are the transfer functions relating the sound pressure and power;

the subscript *m* indicates the field point corresponding the *m*th span of multiple span bridges, which will be explained later.

Assuming the transfer function $H_{\mathrm{r},m}$ is independent of the distribution of forces on the structure, the sound pressure produced by the vibration of the rail subjected to roughness excitation at multiple wheels can be expressed as

$$p_{\mathrm{r},m}^2 = W_{\mathrm{sr}} H_{\mathrm{r},m};\ p_{\mathrm{b},m}^2 = W_{\mathrm{sb}} H_{\mathrm{b},m} \tag{7}$$

where W_{sr} and W_{sb} are given by Eq. (5). Eq. (7) can be written as

$$p_{\mathrm{r},m}^2 = \langle \bar{v}^2 \rangle_{\mathrm{r}} \frac{\hat{p}_{\mathrm{r},m}^2}{\langle \hat{\bar{v}}^2 \rangle_{\mathrm{r}}}, \qquad p_{\mathrm{b},m}^2 = \langle \bar{v}^2 \rangle_{\mathrm{b}} \frac{\hat{p}_{\mathrm{b},m}^2}{\langle \hat{\bar{v}}^2 \rangle_{\mathrm{b}}} \tag{8}$$

Eq. (8) contains the ratio of the rail (or bridge) vibration obtained from the coupled wheel-track-bridge model to that obtained from the acoustic model subjected to the given set of unit point forces. These ratios are thus used to scale the sound pressures obtained from the acoustic model.

3.3 Noise from multiple spans

The three-dimensional vibro-acoustic model for the noise prediction includes the bridge or rails in a single span. However, the noise in the far field is influenced by multiple bridge spans that are excited into vibration during the passage of the train. As shown in Fig. 5, the noise at a given field point P0 from multiple spans during the passage of a train is composed of the sound radiated from bridge spans B0, B1, B2, B3 etc. on the left of the field point and B1', B2', B3' etc. on the right. With the single span acoustic model, this study takes advantage of the principle of reciprocity to consider the effect of multiple bridge spans.

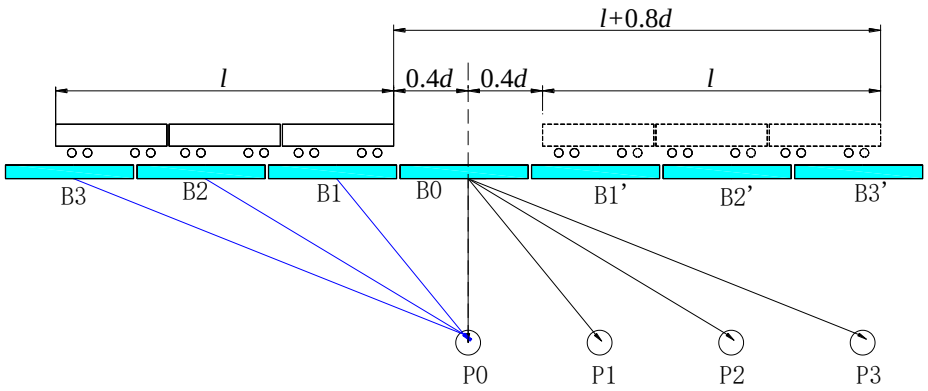

Fig. 5. Noise from multiple spans during the pass-by of a train. *l* is the length of the train and *d* is the perpendicular distance of the field point from the track centre line

The sound pressure produced by a multi-span bridge can be calculated from the weighted summation of the sound energy from each span. This assumption is reasonable because the rail roughness on each span can be regarded as incoherent. Using the principle of reciprocity, the mean square sound pressure at a given field point P0 opposite the middle of bridge span B0 and produced by vibration of span B*m* is equal to that at the field point opposite the middle of bridge span B*m*' but produced by span B0, see Fig. 5.

This approach is only valid when each span is excited into vibration by the train with the same magnitude. For a multi-span rail bridge with equal span lengths, the train is present on each span for the same length of time but it moves from one span to another during the passage of the train. As a result, the sound pressure produced by a multi-span bridge can be calculated using the weighted summation of sound energy from each span

$$p_{\mathrm{b}}^2 = \frac{1}{t_{eq}} \sum_{m=-M}^{M} t_m \tilde{p}_{\mathrm{b},m}^2 \tag{9}$$

where $\tilde{p}_{\mathrm{b},m}^2$ denotes the sound pressure at the field point P0 opposite the mid-span of span B0 due to vibration of span B*m*; t_m is the time during which the train is present on the *m*th

span; t_{eq} is the total pass-by time of the train, which is defined based on the running distance of l+0.8d shown in Fig. 5, according to the Chinese standard [35], where l is the length of the train and d is the perpendicular distance of the field point from the track centre line; 2M+1 is the total number of spans that are directly excited by the moving train during the pass-by time; the mid-span of span B0 is regarded as the plane of interest. The value of M is determined according to the number of bridge spans within the length of the train. For instance, for a train of length 132 m and multiple simply-supported bridge spans of length 30 m, M can be approximately set to 4 (≈132/30).

The aforementioned procedure for noise prediction will be validated by comparison with field measurements in Section 4.4.

4 Validation

4.1 Applicability of the power balance method

A simply-supported single-track bridge with U-shaped section (Fig. 6a) and length 30 m was chosen to investigate the accuracy of the mean-square vibration calculated from the power balance formula (Eq. (2)). The maximum element size in the finite element model was 200 mm (Fig. 6b), which is sufficiently small compared with the structural wavelength (about 2.0 m) of vibration modes of the bridge at around 1000 Hz. This model is used to obtain the mobilities at the positions of the rail fasteners using the modal superposition method and including the modes of vibration up to 1280 Hz. The Young's modulus of the concrete used for the bridge is 40 GPa and its density is 2600 kg/m^3; the damping loss factor of the bridge is 0.04. The rail bearing blocks and other equipment on the bridge were omitted in this section for simplicity. Fig. 7 gives some typical mode shapes and natural frequencies of the bridge. It can be noticed the

bridge exhibits many high-order vibration modes at frequencies of dozens and hundreds of Hertz. Fig. 8 shows the number of modes and modal overlap factor [9] of the bridge in each 1/3 octave band. It can be seen from the figure that the modal overlap factor exceeds 0.3 above 40 Hz and 1.0 above 80 Hz, which can be regarded as the lower limits of the mid-frequency and high frequency ranges [36, 37].

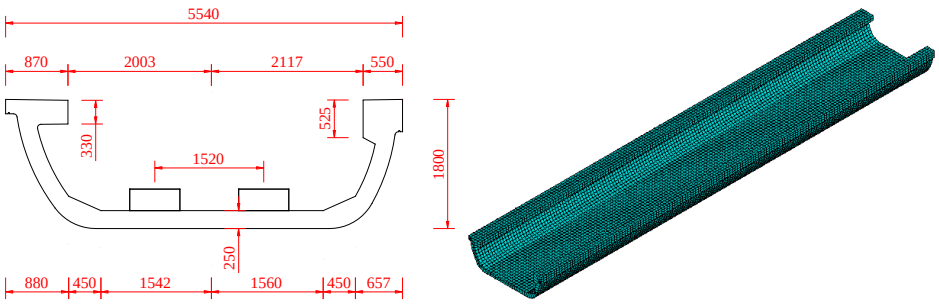

(a) (b)

Fig. 6. Sectional views of the U-shaped bridge at the middle span (unit: mm) and the finite element model: (a) sectional view; (b) finite element model

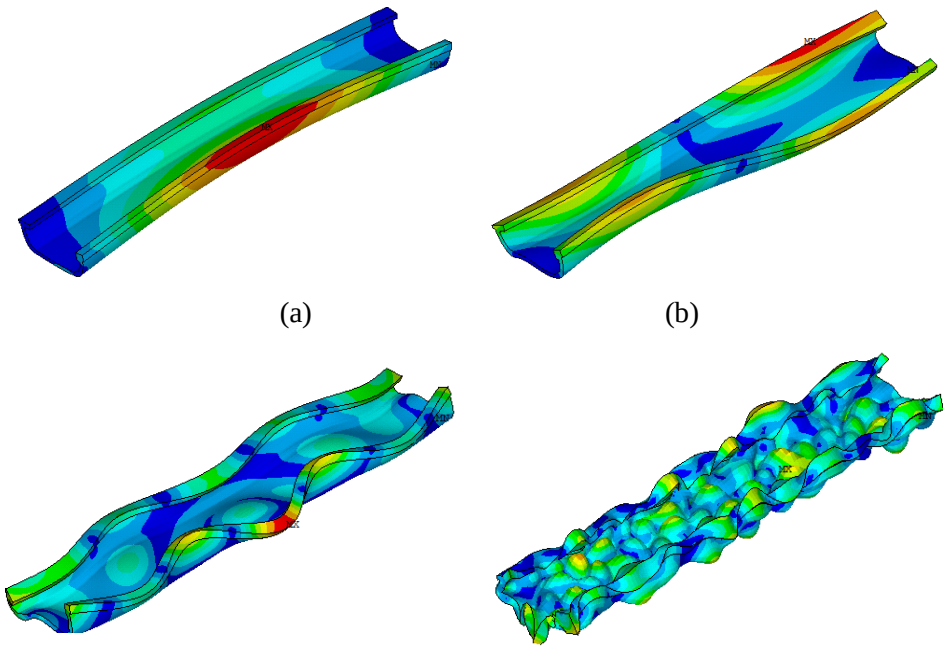

(a) (b)

(c) (d)

Fig. 7. Example mode shapes of the U-shaped bridge: (a) the 1st mode, 4.23 Hz; (b) the 3rd mode, 11.49 Hz; (c) the 25th mode, 60.13 Hz; (d) the 400th mode, 693.16 Hz

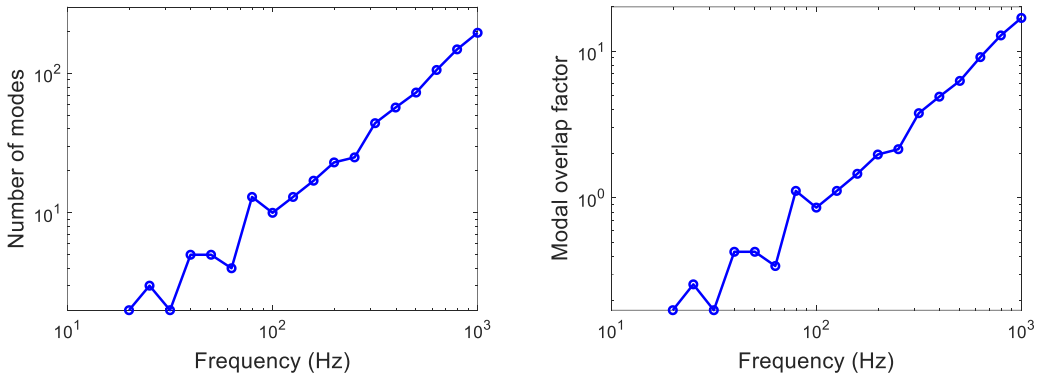

Fig. 8. Number of modes and modal overlap factor of the bridge in each 1/3 octave band: (a) number of modes; (b) modal overlap factor

To check the accuracy of the power balance method for bridge vibration analysis, numerical summation was used to calculate the spatially averaged vibration of the bridge by using the following definitions

$$\langle \bar{v}^2 \rangle_{\mathrm{m}} = \frac{1}{2A} \sum_{i=1}^{N_{\mathrm{a}}} A_i \left[\left(\sum_{j=1}^{M_i} \frac{v_{ij,\mathrm{x}}}{M_i} \right)^2 + \left(\sum_{j=1}^{M_i} \frac{v_{ij,\mathrm{y}}}{M_i} \right)^2 + \left(\sum_{j=1}^{M_i} \frac{v_{ij,\mathrm{z}}}{M_i} \right)^2 \right] \tag{10}$$

$$\langle \bar{v}^2 \rangle_{\mathrm{n}} = \frac{1}{2A} \sum_{i=1}^{N_{\mathrm{a}}} A_i \left[n_x \sum_{j=1}^{M_i} \frac{v_{ij,\mathrm{x}}}{M_i} + n_y \sum_{j=1}^{M_i} \frac{v_{ij,\mathrm{y}}}{M_i} + n_z \sum_{j=1}^{M_i} \frac{v_{ij,\mathrm{z}}}{M_i} \right]^2 \tag{11}$$

where $\langle \bar{v}^2 \rangle_{\mathrm{m}}$ denotes the spatially averaged mean-square total vibration regardless of the vibration direction and $\langle \bar{v}^2 \rangle_{\mathrm{n}}$ is the vibration calculated from the normal velocity of each external elemental face (which is more relevant to noise radiation); N_{a} is the total number of element faces of the bridge in contact with the air; M_i is the number of nodes on the *i*-th face, and A_i is the area of the face (see Fig. 9); $A = \sum A_i$ is the total area of the external surface of the bridge; $v_{ij,\mathrm{x}}$, $v_{ij,\mathrm{y}}$ and $v_{ij,\mathrm{z}}$ are the magnitudes of vibrational velocity components of the *j*-th node on the *i*-th element face in the global *x*, *y* and *z* coordinates; n_x, n_y and n_z are the components of the unit normal vector of the *i*-th element face; the factor 2 in the denominator is used to convert the square of the velocity amplitude to the (temporal) mean square velocity.

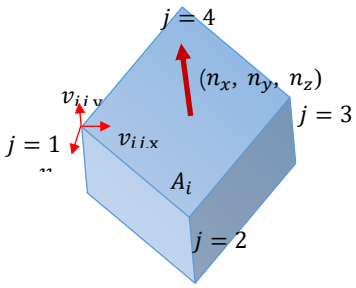

Fig. 9. Schematic diagram of the global and normal vibration of an elemental surface in contact with the surrounding air

In this study, the vibration and sound radiation of the bridge and the rail are calculated at the centre frequencies of 1/9 octave bands and the results are then converted to and displayed in one-third octave bands. Fig. 10 compares the velocity levels of the U-shaped bridge obtained from the various methods, i.e. the power balance method, Eq. (2), the numerical calculation of the total vibration, Eq. (10) and the numerical calculation of the normal velocity, Eq. (11). In the FE model, a unit force was applied at different longitudinal locations of the rail to excite the bridge through fastener forces. The origin of the *x* coordinate is taken to be at the bridge centre. The stiffness and damping loss factor of the fastener are 40 MN/m and 0.15 respectively. The damping loss factor of the rail is set to be 0.04 to match the track decay rate estimated from measured rail acceleration [7]. Fig. 11 gives the level difference between the results from the different methods. It can be observed from Fig. 10 and Fig. 11(a) that the power balance formula (Eq. (2)) gives a good prediction (error within 0.5 dB) of the overall bridge vibration. However, the direct use of the power balance formula overestimates the normal vibration of the bridge, although the errors are less than 3 dB in all frequency bands. The errors generally decrease at higher frequency with the increase of the modal overlap factor. Above 400 Hz the errors increase again slightly because in the high frequency range there are more modes of vibration in the plane of the bridge panels that also dissipate energy. These modes contribute to the

tangential vibration but are not included in the normal vibration of the bridge surface. These results show that the power balance method can be used to calculate the vibration of a concrete bridge above 20 Hz with acceptable accuracy.

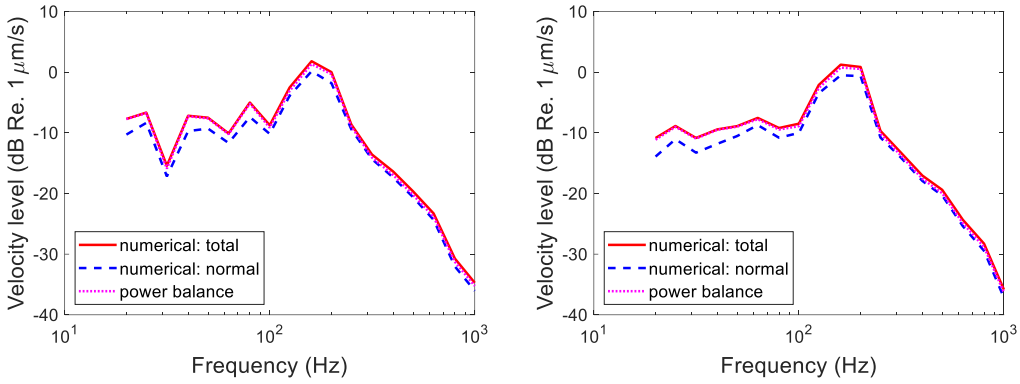

Fig. 10. Spatial averaged velocity of the bridge obtained from various methods and excited by a unit force at different rail location: (a) x=0 m; (b) x=7.2 m

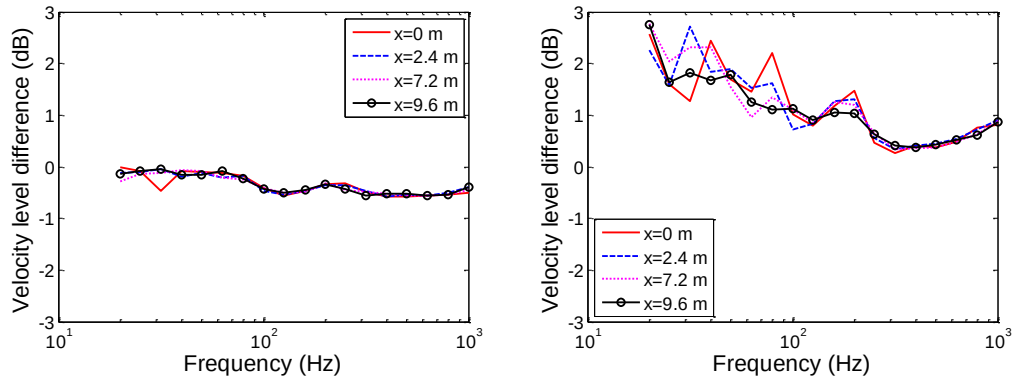

Fig. 11. Difference of spatial averaged velocity level of the bridge from various methods excited by a unit force at different rail locations: (a) difference between power balance method and numerical calculation of total velocity; (b) difference between power balance method and numerical calculation of normal velocity

4.2 Effect of adjacent wheels

The railway vehicle used in this study has a length of 22.8 m, a wheelbase of 2.4 m and a bogie centre distance of 15.6 m. The mass of each wheelset is 1663 kg. The span of a simply-supported bridge with length 30 m can usually accommodate at least four wheelsets as the train

passes over the bridge. The effect of additional wheels on the adjacent spans is discussed in this section and compared with considering only four wheels (x= -4.8, -2.4, 2.4, 4.8 m, where x=0 is at the centre of the span). The rail-bridge model comprising three spans of simply-supported U-shaped bridges is used to together with another two (x=-18, 18 m) or four wheels (x=-18, 18, -20.4, 20.4 m) on the adjacent bogies. Fig. 12 gives the vibration level difference of the rail and bridge excited by incoherent roughness excitations and with different numbers of wheels on the rail compared with the results obtained using four wheels on the centre span of the bridge. The vibration of the rail and bridge was calculated based on the energy superposition principle. Fig. 12(a) shows the rail vibration within the span of interest is mainly influenced by the four wheels that are closest together (the four wheels from two bogies of adjacent vehicles). The difference induced by the wheels located off the span of interest only have slight influence on the averaged rail vibration when the track decay rate is low above 300 Hz. It can be also observed from Fig. 12(b) that the simplified model with four wheels on the bridge produces negligible errors in the bridge vibration compared with those with more wheels. This is because the power input to the bridge span of interest is mainly controlled by the wheels on that bridge and the wheels on other spans have insignificant effect. Therefore, in the following calculations use is made of four wheels sitting on the single bridge span.

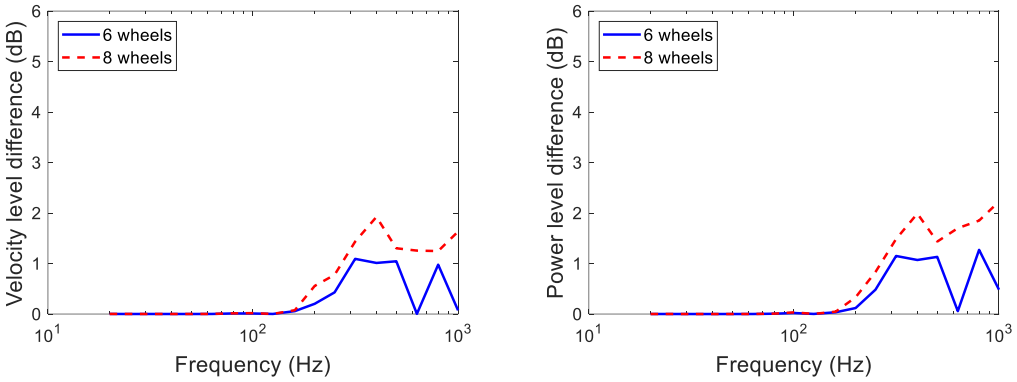

(a) (b)

Fig. 12. Vibration level difference of the rail and bridge of interest excited by 6 or 8 wheels compared with the result for 4 wheels: (a) rail; (b) bridge

4.3 Effect of coherence of roughness excitation

The effect of the phase of the roughness is investigated in this section, namely by comparing coherent roughness and incoherent roughness. The wheel-rail-bridge model consists of four wheels and one bridge span. A roughness of 0 dB relative to 1 μm at each 1/9 octave wavelength was used to excite the coupled system. The responses in 1/9 octave bands are then averaged to obtain the results in 1/3 octave bands.

Fig. 13 compares the wheel-rail contact force and rail vibration produced by four wheels obtained using different roughness excitation methods for a train speed of 80 km/h. For the coherent roughness assumption, the phase of the roughness is related to the wheel location. The result for incoherent excitation is the average from 50 samples of roughness of the same amplitude but random phases at each wheel. It can be seen from Fig. 13(a) that the averaged wheel-rail contact forces obtained from the energy superposition method agree well with those for random incoherent roughness excitation. The coherent excitation generally gives a similar result to the incoherent excitation except at the frequency bands of 630 Hz and 1000 Hz. However, the spatially averaged rail vibration is significantly overestimated by the energy

superposition method above 630 Hz, as can be observed from Fig. 13(b). This is because the rail vibration produced from different wheels is coherent due to the coupled vibration of the wheel-rail system in the high frequency range where the track decay rate is very low. The rail vibration is overestimated by the energy summation principle because it omits the wave interference effect which reduces the rail vibration at a certain distance. Fig. 13(b) shows the rail vibration from the incoherent and coherent roughness assumptions are very similar if the complex wheel-rail forces are used to calculate the rail vibration. It is therefore suggested to use coherent roughness excitation on various wheels to obtain the complex wheel-rail forces and then calculate the rail and bridge vibration using the complex forces. This has sufficient accuracy while avoiding calculations with large numbers of random samples of roughness.

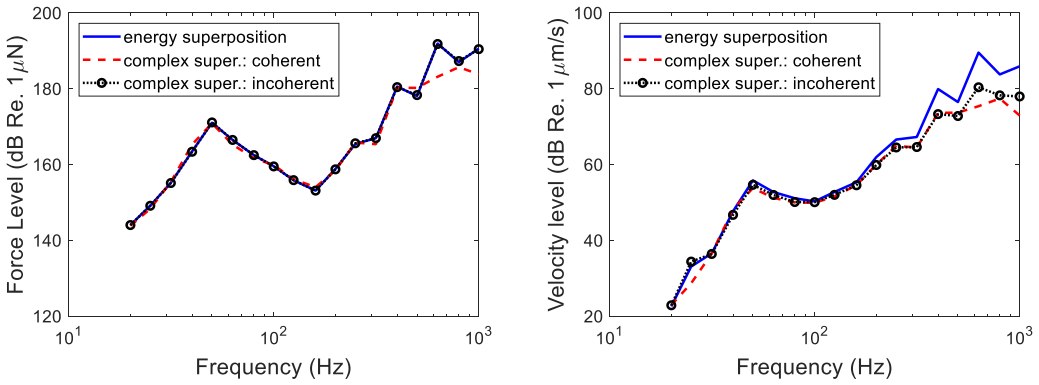

(a) (b)

Fig. 13. Comparison of wheel-rail contact force and rail vibration with the wheel-rail-bridge coupled model using different methods at the speed of 80 km/h: (a) wheel-rail contact force; (b) spatially averaged rail vibration

4.4 Comparison with measured results

In this section the method developed for noise prediction is validated by comparison with noise measured in the field for the U-shaped concrete bridge shown in Fig. 6(a). The rail bearing blocks and the mass of other equipment on the bridge were included in the model in this section to obtain higher accuracy. The wheel-rail combined roughness was estimated from the

measured rail vibration similarly with the method used in Refs. [7, 38]. Fig. 14 shows the estimated wheel-rail combined roughness level (reference to 1 μm) together with the limit curve for vehicle type tests in ISO 3095: 2013 [39]. The roughness at each wheel position was assumed to be correlated, with the phase chosen according to the wheel positions. Two typical wheel cases (four wheels from one vehicle and four wheels from two adjacent bogies, in each case located symmetrically with respect to the bridge centre) are considered to calculate the average rail and bridge vibration.

Fig. 15 gives the predicted noise from the U-shaped girder bridge at 7.5 m and 25 m away, opposite the bridge centre, at a height of 1.5 m above the top of the rails. The acoustic model shown in Fig. 4 is used for the calculation of the sound pressure transfer functions at the field points. It can be seen that the rail noise exceeds the bridge noise above 250 Hz. Fig. 16 compares the predicted total noise with the measured one. It can be observed that the predicted noise generally matches the measured one in trend over a wide frequency range, although the prediction exceeds the measurement below 125 Hz and is lower than the measurement above this frequency. The higher levels at low frequencies are in part due to the overprediction of the surface velocity by the power balance approach (Fig. 11(b)). Having validated this noise prediction method, the noise from bridges of different sections will be compared in the next section for the purpose of low noise bridge construction.

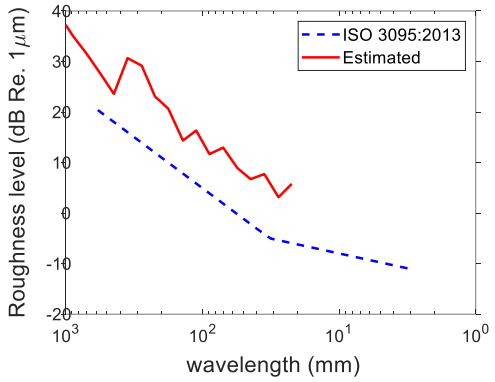

Fig. 14. Estimated wheel-rail combined roughness level together with the limit curve for vehicle type tests from ISO 3095:2013

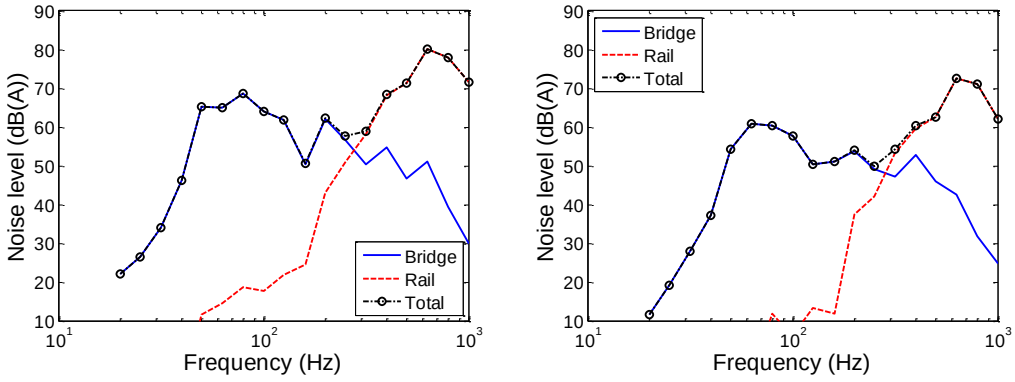

(a) (b)

Fig. 15. Predicted rail, bridge and total sound pressure levels from the U-shaped bridge at the speed of 80 km/h: (a) 7.5 m away and 1.5 m above the rail centre; (b) 25 m away and 1.5 m above the rail centre

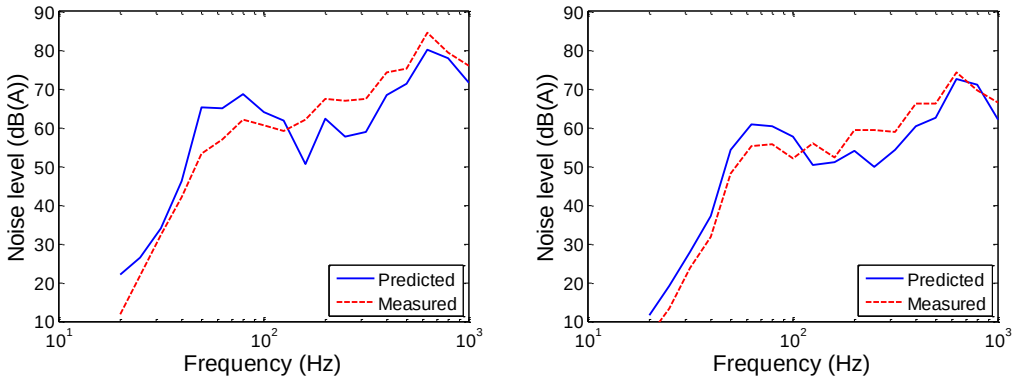

(a) (b)

Fig. 16. Predicted and measured total sound pressure levels from the U-shaped bridge at the speed of 80 km/h: (a) 7.5 m away and 1.5 m above the rail centre; (b) 25 m away and 1.5 m above the rail centre

5 Comparison among various bridge sections

Besides the U-shaped girders (referred to in the following as bridge A), box girders are widely applied in elevated rail transit traffic. To investigate the vibration and noise properties of elevated bridges with different sectional types, comparative results will be shown for a box girder bridge with a single cell (bridge B) and a twin-box girder bridge with two cells (bridge C) as depicted in Fig. 17(a) and 17(b). These three bridges are all designed for the same span length of 30 m. Their material properties including the damping are all assumed to be the same as considered earlier for the U-shaped girder. The masses of the three bridges are 238 tonnes, 448 tonnes, and 506 tonnes respectively; the latter are double track bridges whereas the U-shaped girder is a single track bridge. Their radiating surface areas are 520 m^2, 552 m^2, and 780 m^2 respectively. The same estimated roughness spectrum shown in Fig. 14 is adopted for all three bridges to allow direct comparison; the train speed is 80 km/h in each case.

The webs of the U-shaped girder can work as both noise barriers and crash barriers. Additional crash barriers are often installed on the sides of the box girders to contain trains in case of a derailment. For the present comparison the height of the crash barriers on the box girders are set to be 1.0 m above the top of the rail, which is equivalent to the height of the top of the U-shaped girder. The crash barriers on the box girders can also work as noise barriers. This effect is therefore taken into account but the vibration of the barriers is neglected since their lateral vibration is generally small compared with the vertical vibration of the deck plates. As Bridge B is designed for a train with a smaller car body, the width of the deck is smaller than that of Bridge C. However, to maintain the equivalence between them, the sound pressure transfer functions for the rail noise of Bridge B are taken to be the same as those for Bridge C.

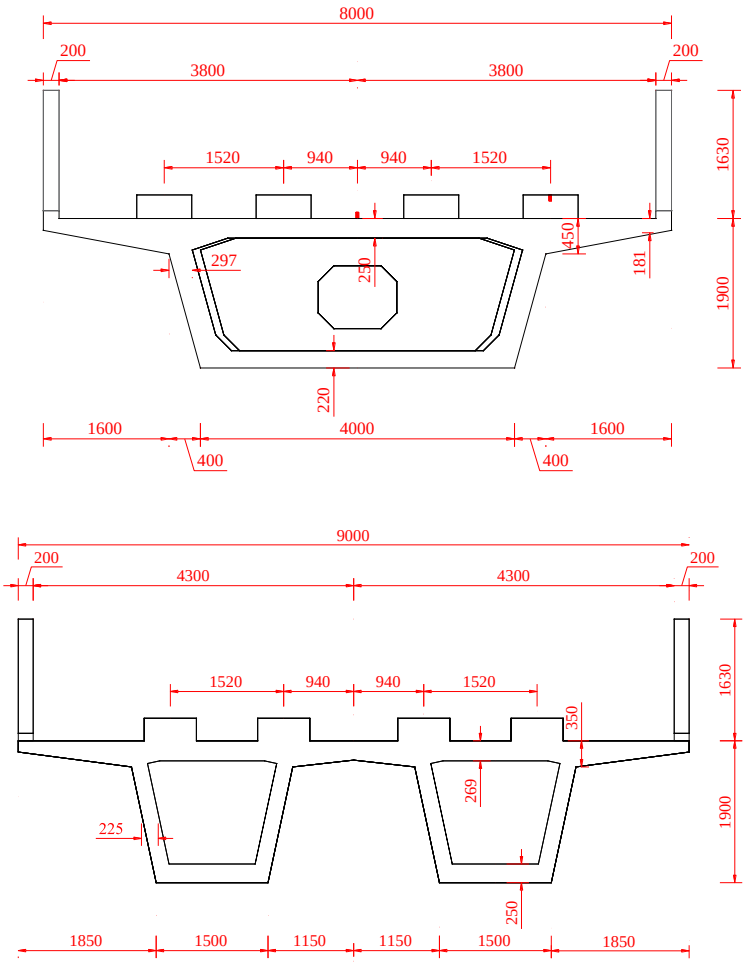

(a) (b)

Fig. 17. Sectional views of two box girder bridges at the middle span (unit: mm): (a) single cell box girder (bridge B); (b) twin-box girder with two cells (bridge C)

Fig. 18(a) compares the driving point mobilities on the outer rails at 2.4 m from the mid-span for the three bridges, and Fig. 18(b) shows the track decay rates of the track in each case, calculated according to the EN standard [40]. It can be seen that the bridges have little influence on the track vibration above 200 Hz. At frequencies below 100 Hz, the mobilities of the rail on bridge A can be up to 1.3 times greater than those for the other two bridges, and the track decay rate for bridge A is about a factor of 1/3 smaller than those for the other two bridges. This is owing to the lower stiffness of the deck of the U-shaped girder compared with the decks of bridges B and C.

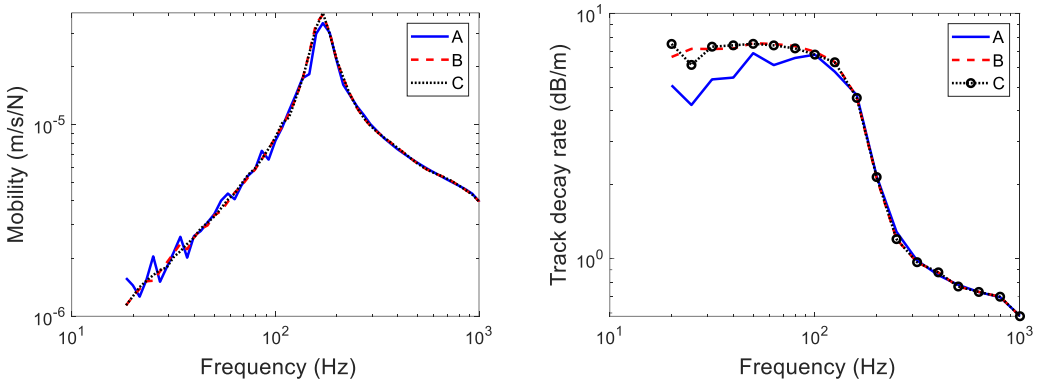

(a) (b)

Fig. 18. Driving point mobilities and track decay rates under the situations of the various bridges: (a) driving point mobilities on the rail; (b) track decay rates

Fig. 19 compares the driving point mobilities of the bridge under the two rails of one track at 2.4 m from the mid-span for the three bridges. The bridge mobilities show large differences between the three bridges, although they are all much smaller than the rail mobilities. The mobilities under the outer rail of bridge B, which are near the vertical web of the girder, are generally smaller than those under the inner rail. As larger bridge mobilities cause larger vibrational power to be transmitted to the bridge, the average power input to bridge A will be the largest at most frequencies, followed by bridge B and C, when excited by the same roughness.

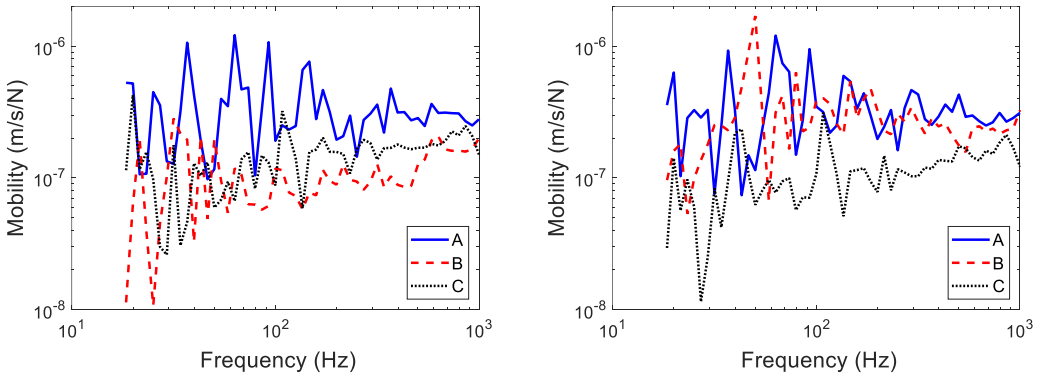

(a) (b)

Fig. 19. Driving point mobilities at 2.4 m from the mid-span of the various bridges: (a) under the outer rail; (b) under the inner rail

Fig. 20(a) shows a comparison of the wheel-rail contact vertical forces at the second wheel, and Fig. 20(b) gives the average total vibration level of the three bridges (calculated from Eq. (2)) for 8 wheels of a vehicle subjected to a roughness of level 0 dB (relative to 1 μm) at each wavelength. It can be observed that the wheel-rail contact forces are virtually unaffected by the bridge design. However, the bridge vibration level of bridge A is about 6 dB larger than that of bridge B around the peak at 50 Hz. This peak frequency corresponds to the resonance of the wheel mass on the stiffness of the track [24]. The vibration level of bridge C is similar to that of bridge B below 100 Hz but is about 3 dB lower than that of bridge B above 100 Hz.

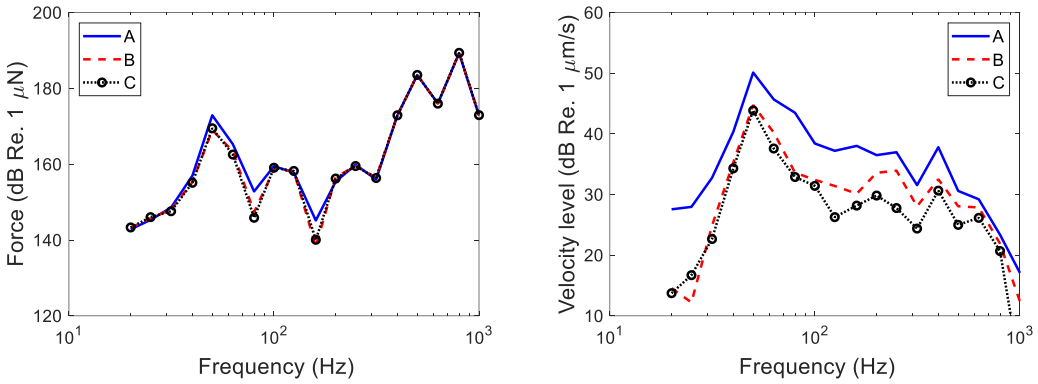

Fig. 20. Wheel-rail contact forces and vibration levels for various bridges for unit roughness: (a) typical wheel-rail contact forces; (b) velocity levels of bridges

Fig. 21(a) depicts the radiation efficiency of the three bridges subjected to specific loads on the bridges. The U-shaped bridge has a lower radiation efficiency than the box girders below 80 Hz. This is because the U-shaped bridge has the smallest plate thickness and largest critical frequency, at around 70 Hz. In addition, the radiating area of the U-shaped girder is smaller than that of the box girders. As a result, the radiated power of the U-shaped bridge, shown in Fig. 21(b) for combined wheel-rail roughness of 0 dB, is only slightly larger (about 1.4 dB) than that of the box girders at the peak at 50 Hz, despite the higher velocity level. However, the radiated power of the U-shaped bridge is 2-8 dB larger than the box girders between 63 Hz and

500 Hz. This has a significant effect on the noise levels at various field points when the actual roughness is considered later.

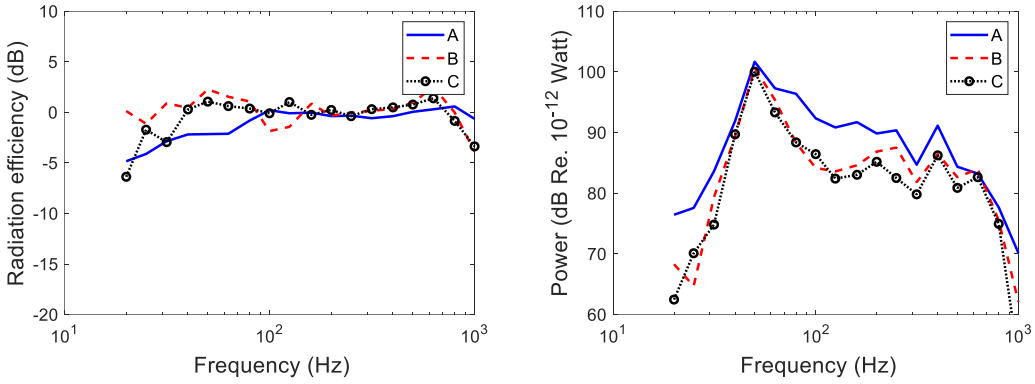

(a) (b)

Fig. 21. Radiation efficiency and power of various bridges: (a) radiation efficiency; (b) radiated power for unit roughness

To investigate the difference in the sound radiated to the far field, 10 field points are defined. Positions S1 to S5 are located 10 m below the top of rail at distances of 7.5, 25, 50, 100 and 200 m from the nearest track centre. Positions S6 to S10 are at 5 m above the top of rail at the same horizontal distances.

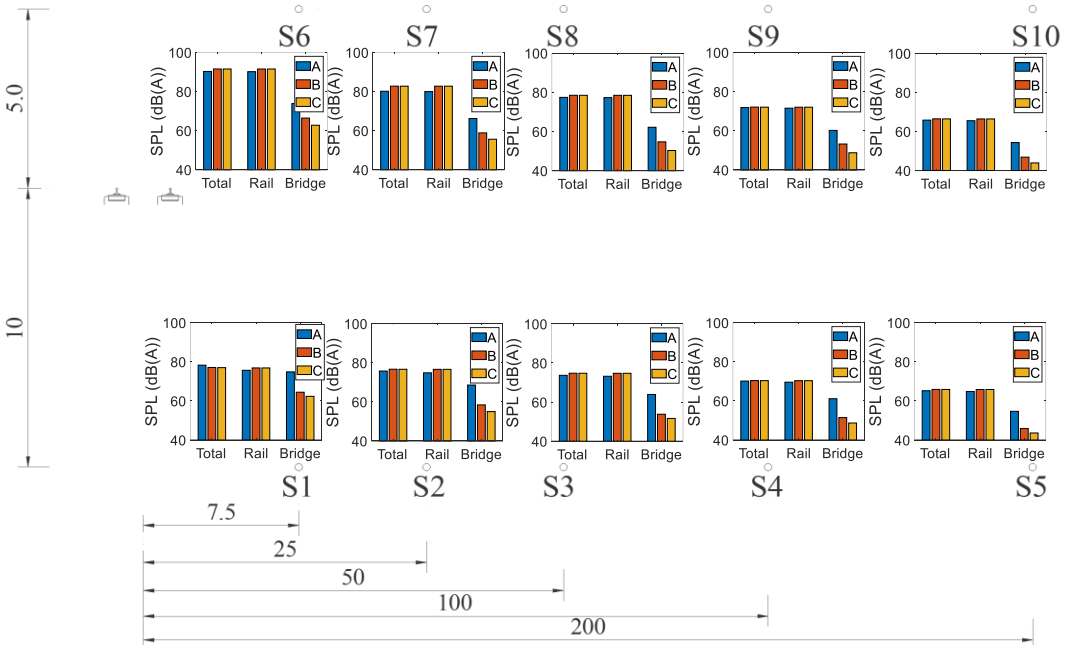

Fig. 22. A-weighted total, rail and noise levels comparison among bridges A, B and C at various field points from S1 to S10

Fig. 22 compares the overall A-weighted noise levels among bridges A, B and C subjected to the same estimated roughness level shown in Fig. 14 at the speed of 80 km/h. The A-weighted total noise levels from bridges B and C are about 0.8 dB larger than that from Bridge A for most positions. The difference in rail noise levels has a similar tendency to the total noise. This difference is mainly caused by the shape and location of the barriers (the U-shaped girder has the smallest gap between the car-body and the barrier) although the heights of the barriers above the rail are the same in each case. The differences in A-weighted bridge noise are larger, with differences of up to 12 dB. Generally, the box girders radiate significantly less bridge noise than the U-shaped girder. The average difference over all positions relative to bridge A is 8.6 dB for bridge B and 11.7 dB for bridge C. Despite these large differences in bridge noise, the total A-weighted noise levels do not have obvious differences because the rail noise is about 10 dB larger than the bridge noise for the three bridges in this study at most of the positions considered.

Fig. 23 shows the A-weighted total noise spectra at various field points for the three bridges. The noise levels are quite similar above 250 Hz where the rail noise dominates. The U-shaped girder produces the largest low frequency noise below 250 Hz where the bridge noise controls the total noise. The double cell box girder (bridge C) generally has the best noise performance.

The low frequency peak in the noise spectra is not always at 50 Hz, as found in Fig 21. This is because the estimated roughness level corresponding to 63 Hz is about 7 dB larger than that corresponding to 50 Hz, as indicated in Fig. 14. It is clear that the comparison of overall noise from different bridges depends on the roughness spectra used in the prediction.

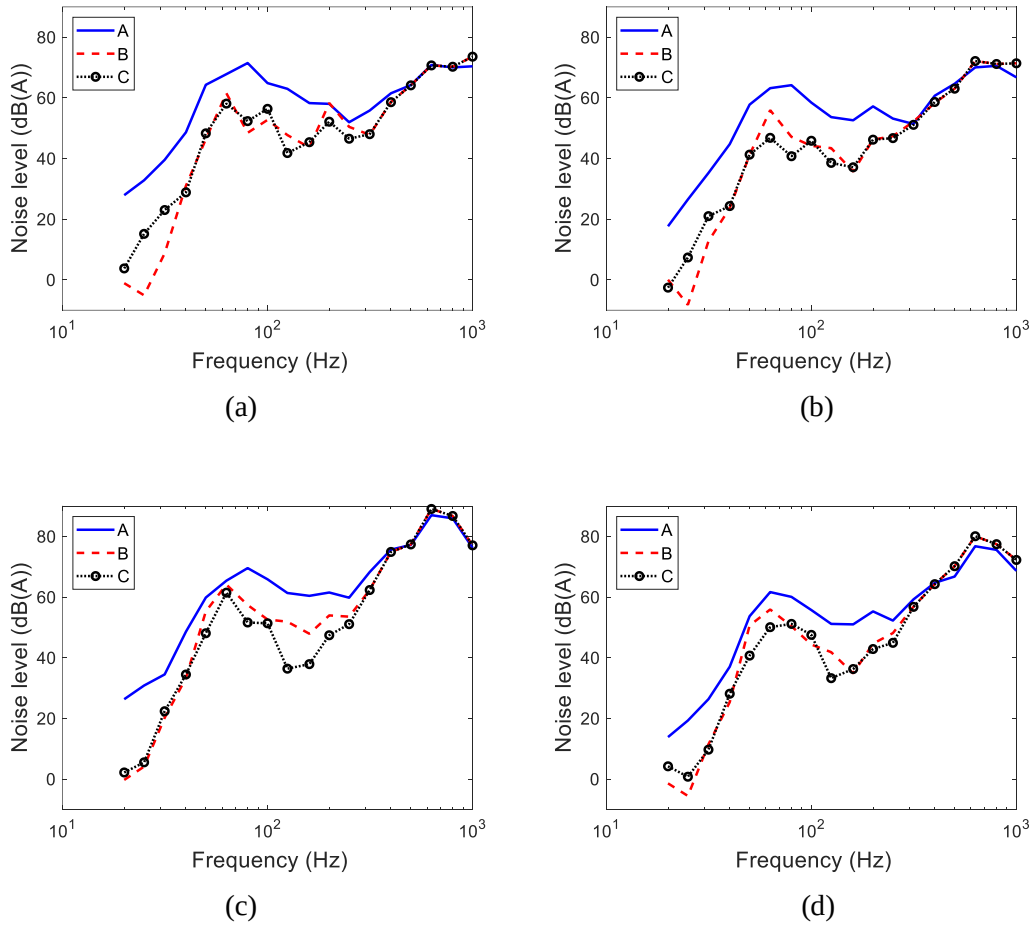

Fig. 23. Total noise level comparison among bridges A, B and C at positions: (a) S1 (7.5 m, -10 m); (b) S2 (25 m, -10 m); (c) S6 (7.5 m, +5 m); (d) S7 (25 m, +5 m)

Fig. 24 shows the A-weighted bridge noise spectra at various field points for the three bridges. It can be seen that the U-shaped girder produces the largest noise level in the whole frequency range. The double cell box girder generally has the best noise performance at dominant frequencies.

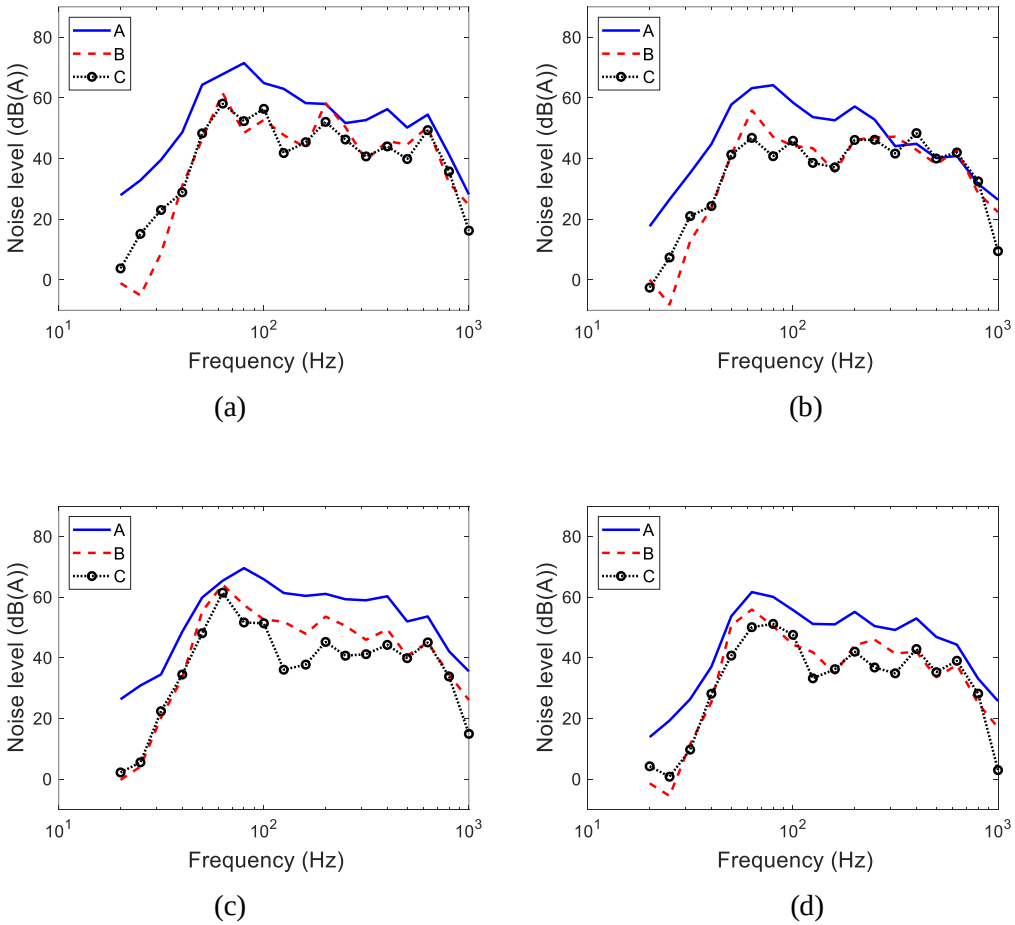

Fig. 24. Bridge noise level comparison among bridges A, B and C at positions: (a) S1 (7.5 m, -10 m); (b) S2 (25 m, -10 m); (c) S6 (7.5 m, +5 m); (d) S7 (25 m, +5 m)

6 Conclusions

An engineering vibro-acoustic model is proposed to predict the noise caused by the passage of a train over a bridge. This is based on a conventional coupled vibration analysis. However, it uses the power balance method to give an efficient estimate of the mean-square velocity. The method developed for noise prediction is based on separate acoustic FE models for the rail noise and bridge noise. The radiation efficiency and sound transfer functions are assumed to be independent of the actual distribution of forces and are calculated by applying several concentrated forces with unit amplitude and different phases. The modelling approach is shown to be effective, giving results that agree well with field measurements.

From analysis of the spatially averaged velocity level of a 30 m simply-supported bridge with a U-shaped section, the power balance method is demonstrated to give satisfactory prediction of the bridge vibration. Compared with a full calculation the total vibration is estimated very closely whereas the velocity normal to the surface is overestimated by up to 3 dB at low frequencies.

Various methods of applying multiple wheel-rail forces are compared and it is found that the rail and bridge vibration can be predicted within an acceptable range if correlated wheel-rail contact forces are used with their phase related to their relative locations. The excitation from wheels on the adjacent spans is analysed to discuss their effects on the vibration of the bridge of interest (one span). The results show that the wheels on adjacent bridges have negligible influence on the vibration of the bridge under consideration.

The method is finally used to compare the vibration and noise properties of elevated bridges with different sectional types. The U-shaped girder generally produces about 1 dB(A) lower total noise levels than the box girders when they have the same height of noise barriers. However, the rail noise level is about 10 dB larger than the bridge noise for the three bridge designs when averaged over the field positions considered in this study. The total noise is therefore dominated by the rail noise which is mainly influenced by the barrier effect but is not affected by the stiffness of the bridge structure. The single-box and twin box girders produce an average of 8.3 and 11.6 dB(A) less noise from the bridge itself than the U-shaped girder because the mobilities of the U-shaped bridge beneath the rails are greater than those of the box girders. As a result, less power is input to the box girders than to the U-shaped girder. Moreover, the mass of the box girders is larger than the (single track) U-shaped girder, leading to higher

average vibration. However, this effect is partly compensated by their larger radiating areas and radiation efficiency.

The comparison of different modelling approaches gives insight into methods that can be used with high efficiency to provide predictions with engineering precision. The comparison of the noise characteristics of different bridge designs gives clear indications of the most promising approach to minimize noise. The modelling approach could be used further in optimisation of the bridge design taking into account practical constraints.

Acknowledgements

The study was supported by the National Natural Science Foundation of China (No. 51878501 and 52078498), and National Engineering Laboratory for High-speed Railway Construction Technology (Open Fund Project HSR201902). The advice on the validation of the method provided by Professor Tianxing Wu of Shanghai Jiaotong University is gratefully acknowledged.

References

[1] Bao X. Urban Rail Transit Present Situation and Future Development Trends in China: Overall Analysis Based on National Policies and Strategic Plans in 2016-2020. Urban Rail Transit. 2018;4:1-12.
[2] Li Q, Xu YL, Wu DJ. Concrete bridge-borne low-frequency noise simulation based on train-track-bridge dynamic interaction. Journal of Sound and Vibration. 2012;331:2457-70.
[3] Zhang X, Li X, Li X, Liu Q, Zhang Z. Train-induced vibration and noise radiation of a prestressed concrete box-girder. Noise Control Engineering Journal. 2013;61:425-35.
[4] Li Q, Song X, Wu D. A 2.5-dimensional method for the prediction of structure-borne low-frequency noise from concrete rail transit bridges. Journal of the Acoustical Society of America. 2014;135:2718-26.
[5] Song XD, Wu DJ, Li Q, Botteldooren D. Structure-borne low-frequency noise from multi-span bridges: A prediction method and spatial distribution. Journal of Sound and Vibration. 2016;367:114-28.
[6] Song X, Li Q, Wu DJ. Investigation of rail noise and bridge noise using a combined 3D dynamic model and 2.5D acoustic model. Applied Acoustics. 2016;109:5-17.

[7] Li Q, Thompson DJ. Prediction of rail and bridge noise arising from concrete railway viaducts by using a multilayer rail fastener model and a wavenumber domain method. Proceedings of the Institution of Mechanical Engineers, Part F: Journal of Rail and Rapid Transit. 2018;232:1326-46.
[8] Song L, Li X, Zheng J, Guo M, Wang X. Vibro-acoustic analysis of a rail transit continuous rigid frame box girder bridge based on a hybrid WFE-2D BE method. Applied Acoustics. 2020;157.
[9] Lyon RH, DeJong RG. Theory and Application of Statistical Energy Analysis (Second Edition). Boston: Newnes; 1995.
[10] Remington P. Prediction of the effectiveness of noise control treatments in urban rail elevated structures. Journal of The Acoustical Society of America - J ACOUST SOC AMER. 1985;78.
[11] Janssens MHA, Thompson DJ. A CALCULATION MODEL FOR THE NOISE FROM STEEL RAILWAY BRIDGES. Journal of Sound & Vibration. 1996;193:295-305.
[12] Bewes OG, Thompson DJ, Jones CJC, Wang A. Calculation of noise from railway bridges and viaducts: Experimental validation of a rapid calculation model. Journal of Sound and Vibration. 2006;293:933-43.
[13] Zhang X, Li X, Zhang J, Song L, Li Y. A hybrid model for the prediction of low–frequency noise emanating from a concrete box-girder railway bridge. Proceedings of the Institution of Mechanical Engineers Part F Journal of Rail & Rapid Transit. 2016.
[14] Luo WJ, Zhang ZZ, Wu By, Xu CJ, Yang PQ. Prediction and analysis of structural noise of a box girder using hybrid FE-SEA method. Structural Engineering and Mechanics. 2020;75:507-18.
[15] Poisson F, Margiocchi F. The use of dynamic dampers on the rail to reduce the noise of steel railway bridges. Journal of Sound and Vibration. 2006;293:944-52.
[16] Liu Q, Thompson DJ, Xu P, Feng Q, Li X. Investigation of train-induced vibration and noise from a steel-concrete composite railway bridge using a hybrid finite element-statistical energy analysis method. Journal of Sound and Vibration. 2020;471.
[17] Wu T, Liu J. Sound emission comparisons between the box-section and U-section concrete viaducts for elevated railway. Noise Control Engineering Journal. 2012;60:450-7.
[18] Zhang X, Cao Z, Ruan L, Li X, Li X. Reduction of vibration and noise in rail transit steel bridges using elastomer mats: Numerical analysis and experimental validation. Proceedings of the Institution of Mechanical Engineers Part F-Journal of Rail and Rapid Transit. 2020.
[19] Liang L, Li X, Yin J, Wang D, Gao W, Guo Z. Vibration characteristics of damping pad floating slab on the long-span steel truss cable-stayed bridge in urban rail transit. Engineering Structures. 2019;191:92-103.
[20] Lu Z, Li J, Li Q. Vibration Analysis of Coupled Multilayer Structures with Discrete Connections for Noise Prediction. International Journal of Structural Stability and Dynamics. 2020;20.
[21] Li Q, Li WQ, Wu DJ, Song XD. A combined power flow and infinite element approach to the simulation of medium-frequency noise radiated from bridges and rails. Journal of Sound & Vibration. 2016;365:134-56.
[22] Liang L, Li X, Zheng J, Lei K, Gou H. Structure-borne noise from long-span steel truss cable-stayed bridge under damping pad floating slab: Experimental and numerical analysis. Applied Acoustics. 2020;157.
[23] Li Q, Huang HY, Thompson DJ. Comparison of vibration and noise characteristics of urban rail transit bridges with boxgirder and U-shaped sections. In: Degrande G, Lombaert G, hoorickx CV, Reumers P, editors. 13th International Workshop on Railway Noise , 16-20 September 2019. Ghent, Belgium: Notes on Numerical Fluid Mechanics & Multidisciplinary Design; 2021. p. 691-8.

[24] Thompson D. Railway Noise and Vibration: Mechanisms, Modelling, and Means of Control. In: Thompson D, editor. Railway Noise and Vibration: Mechanisms, Modelling, and Means of Control. Oxford: Elsevier; 2009.
[25] Germonpre M, Nielsen JCO, Degrande G, Lombaert G. Contributions of longitudinal track unevenness and track stiffness variation to railway induced vibration. Journal of Sound and Vibration. 2018;437:292-307.
[26] Wu TX, Thompson DJ. On the rolling noise generation due to wheel/track parametric excitation. Journal of Sound and Vibration. 2006;293:566-74.
[27] Nordborg A. Wheel/rail noise generation due to nonlinear effects and parametric excitation. Journal of the Acoustical Society of America. 2002;111:1772-81.
[28] Wu TX, Thompson DJ. Vibration analysis of railway track with multiple wheels on the rail. Journal of Sound and Vibration. 2001;239:69-97.
[29] Li Q, Li WQ, Wu DJ, Song XD. A combined power flow and infinite element approach to the simulation of medium-frequency noise radiated from bridges and rails. Journal of Sound and Vibration. 2016;365:134-56.
[30] Sun W, Zhou J, Thompson D, Gong D. Vertical random vibration analysis of vehicle-track coupled system using Green's function method. Vehicle System Dynamics. 2014;52:362-89.
[31] Lyon RH, DeJong RG. Theory and Applications of Statistical Energy Analysis. Boston Butterworth-Heinemann; 1995.
[32] Putra A, Thompson DJ. Sound radiation from rectangular baffled and unbaffled plates. Applied Acoustics. 2010;71:1113-25.
[33] Li Q, Thompson DJ. Directivity of sound radiated from baffled rectangular plates and plate strips. Applied Acoustics. 2019;155:309-24.
[34] Zhang X, Squicciarini G, Thompson DJ. Sound radiation of a railway rail in close proximity to the ground. Journal of Sound and Vibration. 2016;362:111-24.
[35] MEE. Technical Guidelines for Environment Impact Assessment of Urban Rail Transit. Beijing: China Environmental Science Press; 2018.
[36] Langley RS. A wave intensity technique for the analysis of high-frequency vibrations. Journal of Sound and Vibration. 1992;159:483-502.
[37] Denis V, Pelat A, Gautier F, Elie B. Modal Overlap Factor of a beam with an acoustic black hole termination. Journal of Sound and Vibration. 2014;333:2475-88.
[38] Li Q, Thompson DJ, Toward MGR. Estimation of track parameters and wheel-rail combined roughness from rail vibration. Proceedings of the Institution of Mechanical Engineers Part F-Journal of Rail and Rapid Transit. 2018;232:1149-67.
[39] ISO 3095: 2013 Railway applications-acoustics-measurement of noise emitted by rail bound vehicles. 2013.
[40] EN 15461: 2008 Railway applications – noise emissions, characterization of the dynamic properties of track sections for pass by noise measurements., in, European Committee for Standardization. Brussels, Belgium 2008.